A computational study of right ventricular mechanics in a rat model of pulmonary arterial hypertension

Oscar O. Odeigah 1 , Ethan D. Kwan 2 , Kristen Garcia 2 , Henrik Finsberg 1 , Daniela Valdez-Jasso 2 and Joakim Sundnes 1,*

¹Simula Research Laboratory, Oslo, Norway

Correspondence*: Joakim Sundnes sundnes@simula.no

2 ABSTRACT

16

17 18

19

20

21

23

24

26

27

Pulmonary arterial hypertension (PAH) presents a significant challenge to right ventricular (RV) function due to progressive pressure overload, necessitating adaptive remodeling in the form of increased wall thickness, enhanced myocardial contractility and stiffness to maintain cardiac performance. However, the impact of these remodeling mechanisms on RV mechanics in not clearly understood. In addition, there is a lack of quantitative understanding of how each mechanism individually influences RV mechanics.

Utilizing experimental data from a rat model of PAH at three distinct time points, we developed biventricular finite element models to investigate how RV stress and strain evolved with PAH progression. The finite element models were fitted to hemodynamic and morphological data to represent different disease stages and used to analyze the impact of RV remodeling as well as the altered RV pressure. Furthermore, we performed a number of theoretical simulation studies with different combinations of morphological and physiological remodeling, to assess and quantify their individual impact on overall RV load and function.

Our findings revealed a substantial 4-fold increase in RV stiffness and a transient 2-fold rise in contractility, which returned to baseline by week 12. These changes in RV material properties in addition to the 2-fold increase in wall thickness significantly mitigated the increase in wall stress and strain caused by the progressive increase in RV afterload. Despite the PAH-induced cases showing increased wall stress and strain at end-diastole and end-systole compared to the control, our simulations suggest that without the observed remodeling mechanisms, the increase in stress and strain would have been much more pronounced. Our model analysis also indicated that while changes in the RV's material properties – particularly increased RV stiffness - have a notable effect on its mechanics, the primary compensatory factor limiting the stress and strain increase in the early stages of PAH was the significant increase in wall thickness. These findings underscore the importance of RV remodeling in managing the mechanical burden on the RV due to pressure overload.

²Shu Chien-Gene Lay Department of Bioengineering, University of California San Diego, La Jolla, CA, United States

Keywords: pulmonary arterial hypertension, right ventricle, cardiac mechanics, finite-element models, gradient-based optimization,

29 data assimilation

1 INTRODUCTION

Pulmonary arterial hypertension (PAH) is a medical condition marked by a persistent elevation in mean

- pulmonary arterial pressure (mPAP). The prolonged elevation in mPAP imposes a significant burden on the 31
- right ventricle (RV), resulting in impaired RV function which can lead to heart failure(Voelkel et al., 2012). 32
- The prognosis of the disease is notably grim, with a median survival time of merely 3-5 years post-diagnosis 33
- (Hurdman et al., 2012). Studies have highlighted the crucial role of RV function as a prognostic indicator 34
- for disease progression, severity, and patient survival (van Wolferen et al., 2007; Howard, 2011; Swift et al., 35
- 2017). The sustained pressure overload on the RV in PAH triggers geometric remodeling in the form of 36
- hypertrophy (Lamberts et al., 2007), altered myocardial contractility (Vélez-Rendón et al., 2018), and RV 37
- free wall stiffening (Rain et al., 2016). These remodeling mechanisms help to maintain cardiac output in 38
- the early stage of PAH, but can eventually lead to a decline in RV function in the later stages of the disease 39
- (Vonk Noordegraaf et al., 2017). 40
- Despite the link between RV function and patient survival in PAH, there has been limited research 41
- attention given to RV remodeling compared to LV remodeling in systemic hypertension (Odeigah et al., 42
- 2022). This limited research has created a knowledge gap in regards to our understanding of how PAH-43
- induced remodeling affects RV function. Studies have shown that concentric hypertrophy is associated 44
- with preserved RV systolic function in the early stages of PAH (Badagliacca et al., 2015). On the other 45
- hand, recent studies have shown that myocardial stiffening, the main contributor to increased RV diastolic 46
- stiffness (Kakaletsis et al., 2023), prevents pathological RV dilation in the early stages of PAH (Kwan 47
- et al., 2021), but can be associated with impaired RV relaxation and diastolic dysfunction as the disease 48
- progresses, making it an important prognostic indicator of disease severity Rain et al. (2013); Trip et al. 49
- (2015).50
- However, the specific alterations in RV mechanics induced by these remodeling mechanisms are still 51
- not well understood. As altered ventricular mechanics can impact myocardial perfusion leading to RV 52
- ischemia (Strauer, 1979; Alter et al., 2016), and can also cause right-to-left ventricular dyssynchrony 53
- (Vonk-Noordegraaf et al., 2013), it is clear that an understanding of how RV mechanics is altered by 54
- PAH-induced remodeling is of significant clinical interest. Furthermore, untangling the relative effects of 55
- geometric remodeling and altered material properties on RV mechanics can potentially unveil new and 56
- independent predictors of disease severity, or at the very least, provide insight into which mechanisms 57
- dominate RV mechanical response. Overall, there is a critical need to investigate the mechanical changes
- 58
- occurring in the RV during the progression of PAH and to understand the relative effects of the different 59
- remodeling mechanisms on RV mechanics. 60
- The present study seeks to integrate experimental data from a rat model of PAH measured over a 12-week 61
- period into a computational model to elucidate RV mechanical changes during the progression of PAH. 62
- We confined our analysis to three time points that exhibited distinct hemodynamic remodeling phenotypes
- reported previously (Kwan et al., 2021). We aim to quantify the impact of geometric remodeling and 64
- changes in right-ventricular myocardium wall properties on chamber mechanics using predictions of wall 65
- stress and strain as indices. The objective is to develop a robust framework to investigate the effects of 66
- PAH-induced remodeling on RV mechanics.

MATERIALS AND METHODS

2.1 **Data acquisition**

68

95

96 97

98 99

100

102

103

104 105

106 107

108

Pulmonary arterial hypertension was induced in rats as described in (Kwan et al., 2021) using the 69 70 well-established sugen-hypoxia (SuHx) model, an animal model that recapitulates vascular remodeling 71 found in PAH patients (Abe et al., 2010). Male Sprague-Dawley rats (7 weeks old and weighing 214±23g) were administered with 20mg/kg of sugen, a vascular endothelial receptor blocker, and kept in 10% O2 72 73 hypoxia for three weeks. The animals were then removed from the hypoxic chamber and returned to 74 normoxia (21% oxygen) where the pulmonary arterial pressures continued to rise. Age-matched animals 75 were kept in normoxia during the entire period to serve as the control group. The animals underwent invasive hemodynamic procedures at 4, 8, and 12 weeks post-SuHx induction. The three time points 76 77 chosen to build three-dimensional biventricular models were based on a study of RV remodeling involving 78 six time points along the disease progression (Kwan et al., 2021). Briefly, we found that after 4 weeks 79 of sugen-hypoxia, rats had significant rise in end-systolic pressures but no changes in ejection fraction, 80 attributed to significant RV hypertrophy. However, later in the disease or rats studied in later weeks of 81 sugen-hypoxia, there were no more changes in hypertrophy. Instead, there was a sharp rise in end-diastolic pressure and end-diastolic elastance with preserved end-diastolic volume. By 12 weeks of sugen-hypoxia, 82 83 animals show a small reduction in RV end-diastolic elastance, in ejection fraction, and a slight increase in volume. Here we sought to investigate these features. While we note a gradual decrease in the RV ejection 84 fraction over 12 weeks (from 65% in the control to 50%, 47%, and 43% after 4, 8, and 12 weeks), the ejection fraction remained above heart failure thresholds of 35-40% (Meyer et al., 2010). 86

Following previously described methods (Vélez-Rendón et al., 2018), all animals underwent invasive 87 open-chest measurements of blood pressure and volume taken in the right and left ventricles while kept 88 under 2.5% isoflurane. Pressure-volume (P-V) timeseries were aligned within the cardiac cycle and 89 90 averaged. End of systole (ES) was determined by identifying the maximum pressure-to-volume ratio 91 point in the P-V loop. The end-diastolic (ED) point was identified as the timepoint in the P-V loop where the pressure was at a minimum and the pressure rate of change (i.e. dp/dt) was at a maximum. After 92 these hemodynamic measurements were taken, the heart was flushed and excised. RV free wall thickness 93 measurements were taken ex vivo across the wall and averaged to obtain a representative RV wall thickness. 94

2.2 Biventricular shape model

Rat-specific meshes were built using data from hemodynamic pressure- volume timeseries and morphological measurements from harvested hearts from four different rats. These rats were selected to represent normotensive and three distinct sugen-hypoxia groups, published in Kwan et al. (2021). The idealized three-dimensional biventricular meshes were built using Gmsh (Geuzaine and Remacle, 2009) and each rat-specific model was parameterized based on the animal hemodynamic and morphological data outlined in Table 1. 101

We adapted the RV wall thickness of each mesh to match the experimentally measured RV wall thickness and inflated both ventricles to match the cavity volumes presented in Table 1. The meshes were then partitioned into two regions representing the right ventricular free wall (RVFW) and the LV region, which consisted of the left ventricular free wall (LVFW) and the interventricular septum. The morphology, myocardium properties and hemodynamics of the LV were kept constant for all cases, as there was no indication of changes in the left ventricle in any of these animals (Kwan et al., 2021). The muscle-fibre architecture was registered on the meshes using the Laplace Dirichlet Rule-Based algorithm (Bayer et al.,

109 2012). We prescribed the myofiber helix angle to vary transmurally from $+60 \deg$ at the endocardium to $-60 \deg$ at the epicardium. In Figure 1, we show the meshes built for each case, along with an example of the mesh partitioning and myocardial fiber registration on the control case mesh.

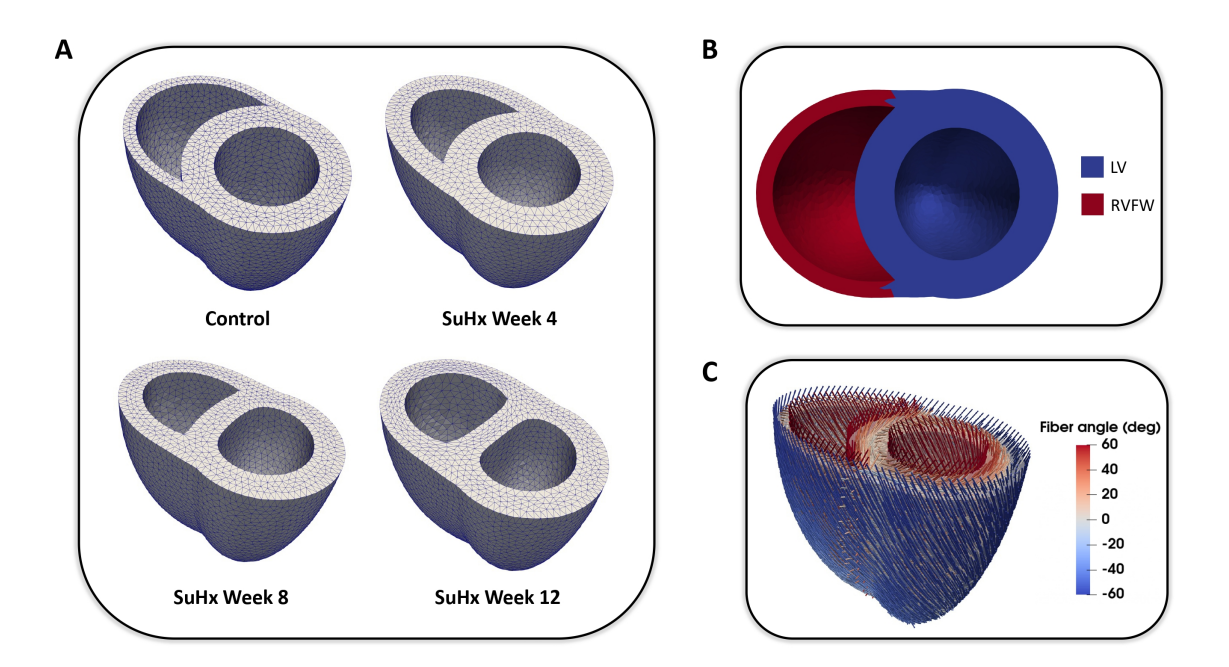


Figure 1. (A): Idealized three-dimensional finite element meshes representing the control, SuHX Week 4, SuHx week 8, and SuHx week 12 cases. (B): Control mesh partitioned into two regions representing the RVFW (in red) and the LV (in blue) which comprises the LVFW and septum. (C): Myocardial fibers embedded in the control mesh using the Laplace Dirichlet Rule-Based algorithm. LV, left ventricle; LVFW, left ventricular free wall; RVFW, right ventricular free wall; SuHx, sugen-hypoxia.

12 2.3 Mathematical modeling

113 We represent the heart as a continuum body, where the coordinates in the reference configuration (X)114 are mapped to coordinates in the current configuration (x) via the deformation gradient:

$$F = I + \nabla u, \tag{1}$$

with u = x - X denoting the displacement of a given point in the domain Ω (i.e., the myocardium). The displacement field is found by solving the quasi-static equilibrium equation given by:

$$\nabla \cdot \boldsymbol{P} = 0, \tag{2}$$

where P is the first Piola-Kirchhoff stress tensor, subject to imposed boundary conditions. The basal displacement of our biventricular domain was set to zero in the longitudinal (apex-to-outflow) direction. Basal movement in the other directions, as well as the movement of the epicardial surface, was restricted by a linear spring of stiffness $k = 0.5 \,\mathrm{kPa/cm^2}$ as in a previous study (Finsberg et al., 2018b). Measured LV

and RV pressures were applied as Neumann boundary conditions at the endocardial surfaces of the domain.

To model the passive behavior of the myocardium, we used the transversely isotropic form of the hyperelastic strain energy function proposed in Holzapfel and Ogden (2009):

$$\Psi(\mathbf{F}) = \frac{a}{2b} \left(e^{b(I_1 - 3)} - 1 \right) + \frac{a_f}{2b_f} \left(e^{b_f \left(I_{4f_0} - 1 \right)^2} - 1 \right), \tag{3}$$

where a, a_f , b, b_f are material stiffness parameters, and the invariants are defined as:

$$I_1 = \operatorname{tr} \boldsymbol{C}, \quad I_{4f_0} = \boldsymbol{f}_0.(\boldsymbol{C}\boldsymbol{f}_0), \tag{4}$$

- 125 with C denoting the right Cauchy Green tensor and f_0 the myocardial fiber direction. We assume the
- 126 myocardium is incompressible and enforce this by adding an extra term p(J-1) to the strain energy
- 127 function with p being a Lagrange multiplier representing the hydrostatic pressure, and $J = \det(\mathbf{F})$.
- To model the active behavior of the myocardium, we applied the commonly used active stress formulation
- 129 (Nash and Hunter, 2000):

$$\sigma = \sigma_n + \sigma_a \tag{5}$$

130 where σ is the total Cauchy stress tensor which is decomposed into a passive stress contribution:

$$\boldsymbol{\sigma}_p = J^{-1} \frac{\partial \Psi}{\partial \boldsymbol{F}} \boldsymbol{F}^T, \tag{6}$$

and an active stress contribution due to the contraction of cardiomyocytes:

$$\sigma_a = T_a \left[(\mathbf{f} \otimes \mathbf{f}) + \eta (\mathbf{I} - \mathbf{f} \otimes \mathbf{f}) \right]. \tag{7}$$

- 132 The magnitude of the active stress is denoted by T_a and η controls the amount of active stress developed in
- 133 the directions transverse to the fiber direction, as studies have shown that active stresses in the transverse
- direction (i.e., sheet and sheet-normal directions) are non-negligible (Lin and Yin, 1998). Similar to the
- 135 study by Sundnes et al. (2014), we have assumed homogeneity in transverse active stress and consequently
- 136 set η to a fixed value of 0.2 (or 20%). Notably, the total Cauchy stress tensor σ and the first Piola-Kirchhoff
- 137 stress tensor P are related by the expression $P = J\sigma^T F^{-T}$.

138 2.4 Model Calibration

- The model was calibrated to match in vivo pressure-volume (P-V) time series data. Measured pressures
 - 40 were provided as input parameters to the model (endocardial boundary conditions), and the model
- 141 parameters were adjusted until the calculated volumes agreed with the measured ones. The model-data
- 142 volume mismatch was defined as

$$\left(\frac{V_{RV}^i - \widetilde{V}_{RV}^i}{V_{RV}^i}\right)^2,$$
(8)

- where \widetilde{V}_{RV} and V_{RV} are the simulated and measured RV cavity volumes, respectively, and i denotes a specific time point.
- Model calibration was carried out in two phases. In the first phase, the passive (isotropic) stiffness
- parameter a in (3) was estimated by fitting the model to P-V data in the passive filling phase of the cardiac
- 147 cycle. Due to the sparsity of data used for the optimization, the remaining three material parameters in
- 148 (3) were not estimated, but fixed to values (b = 5.0, $a_f = 2.582$ kPa, and $b_f = 5.0$) from Finsberg et al.

(2018b) for all simulations in this study. In the second phase, the optimized a parameter was held fixed at its fitted value from the first phase, and the active stress scaling parameter T_a in (7) was estimated by fitting the model to P-V data through the active phases of the cardiac cycle (i.e., isovolumic contraction, ejection and isovolumic relaxation). Since both the P-V values and muscle contraction varies throughout the cardiac cycle, T_a was allowed to vary in time, with a separate value estimated for each measured time point in the cardiac cycle. Figure 2 presents an overview of the parameter estimation pipeline.

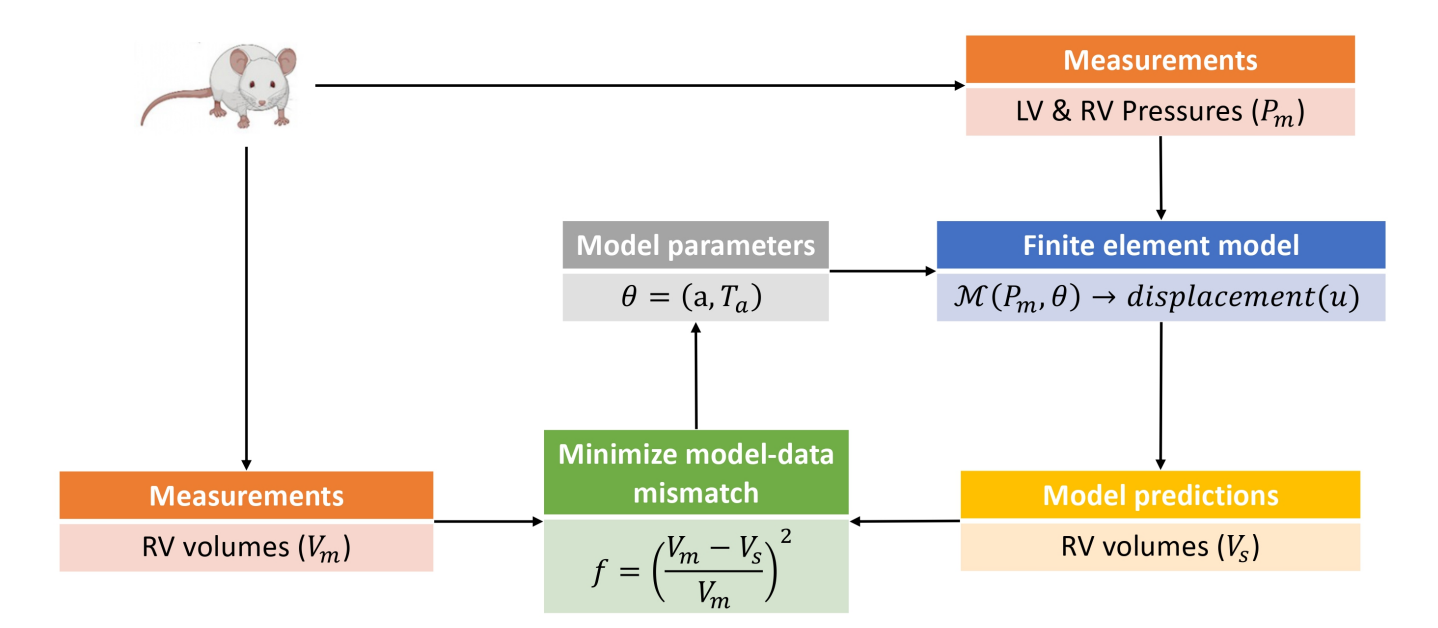


Figure 2. This is a schematic of the parameter estimation pipeline used in this study. The parameter estimation was done in two phases with an estimation of the isotropic scaling parameter a done in the first phase by fitting the model to passive filling pressure-volume data. The second phase involved an estimation of the active stress T_a by fitting the model to pressure-volume data from the active phases of the cardiac cycle. Only model predicted RV volumes were used in the parameter estimation pipeline, as the parameters and hemodynamics for the LV were held fixed for all simulation cases (see Section 2.1). The pressure-volume data was obtained from rats induced with PAH via the sugen-hypoxia (SuHx) protocol, as well as from a control rat. LV, left ventricle; RV, right ventricle.

2.5 Estimation of end-diastolic and end-systolic elastance

End-diastolic elastance (E_{ed}) and end-systolic elastance (E_{es}), proposed as global indices of ventricular stiffness (Templeton et al., 1972) and ventricular contractility (Suga and Sagawa, 1974) respectively, were estimated in this study. These metrics were estimated by perturbing the loading conditions on the optimized model while keeping all other variables fixed. Specifically, at the ED point, the ED pressure P_{ed} was perturbed by incrementing it with a factor ($P_{ed+\Delta} = P_{ed} + \Delta P$), resulting in a change in ED volume ($V_{ed+\Delta} = V_{ed} + \Delta V$). The estimate of ED elastance was then obtained by dividing the change in pressure by the change in volume, given as

$$\widetilde{E}_{ed} = \frac{\Delta V}{\Delta P},\tag{9}$$

where ΔP was set at 0.1 kPa. The same approach was used for estimating E_{es} by perturbing the optimized model at the ES point.

166 2.6 Simulation and implementation details

To solve the set of partial differential equations described in (2), we implemented a Galerkin finite

- 168 element method, which involved discretizing the variational form of (2) using Taylor-Hood tetrahedral
- 169 finite elements (Hood and Taylor, 1974). Specifically, we used piecewise quadratic basis functions for
- 170 the displacement field and piecewise linear basis functions for the hydrostatic pressure field. We used
- a previously developed cardiac mechanics software (Finsberg, 2019) implemented in the FEniCS finite
- 172 element framework (Logg et al., 2012) to solve the numerical problem. For a detailed derivation of the
- variational form of (2), interested readers can refer to the work by Finsberg et al. (2018b).
- 174 For the minimization of the objective function (8) we used the Broyden-Fletcher-Goldfarb-Shanno
- 175 (BFGS) algorithm (Broyden, 1970; Fletcher, 1970; Goldfarb, 1970; Shanno, 1970) implemented in the
- 176 SciPy library (v 1.11.3) (Virtanen et al., 2020) in Python.

3 RESULTS

177

3.1 Model calibration

- 178 The simulated and measured P-V loops for the RV are shown in Figure 3 for the different simulated
- 179 cases. The results show a very good fit between our model and the experimentally measured data. Time
- 180 traces of the optimized active stress parameter T_a are also presented in Figure 3. In addition, we present
- 181 the optimized passive material parameter a for the control, week 4, week 8 and week 12 SuHx cases in
- 182 Table 2. As previous studies have shown no significant change in LV hemodynamics in early-stage PAH
- 183 (Kwan et al., 2021), the same P-V data and material parameters were used for the LV in all simulated cases
- 184 (Figure 4 and Table 2). The LV active and passive material parameters were calibrated using P-V data from
- 185 the control animal.
- We conducted a mesh convergence analysis based on the control geometry and hemodynamics to find the
- optimal mesh resolution needed for accurate model predictions. Specifically, we calculated the average
- 188 Cauchy stress and Green strain employing four distinct mesh resolutions, ranging from a low-resolution
- mesh comprising approximately 5500 elements to a high-resolution mesh comprising approximately 61000
- 190 elements. As depicted in Figure 5, the derived metrics exhibited a very low sensitivity to mesh resolution
- beyond the medium-high resolution (36473 elements) threshold. This observation implies that a mesh
- 192 resolution of 36473 elements is adequate to ensure the accuracy of our model predictions. The chosen
- 193 mesh sizes for the control, 4, 8, and 12 weeks post-PAH analyses are detailed in Table 3, including the
- 194 respective average evaluation time for the cost functional (8), the number of cost-functional evaluations to
- 195 fit one P-V point, and the total run times for each optimization process. All computational analyses were
- 196 conducted on a computing cluster utilizing a single node with 32 cores.

197 3.2 Mechanical analysis

198 3.2.1 End-diastolic and end-systolic elastance

- Table 4 presents the model-predicted end-diastolic elastance (E_{ed}) and end-systolic elastance (E_{es})
- 200 computed by perturbing RV pressure at the ED and ES points respectively, as described in Section 2.5.
- 201 Additionally, we provide a comparison of the model-predicted values with the group means and standard
- 202 errors from animals at the corresponding time points in Kwan et al. (2021). It should be noted that Kwan
- 203 et al. only included animals up to 10 weeks post-PAH induction in their study. As such, the group means
- 204 depicted in Table 4 for week 12 are actually for week 10 animals.

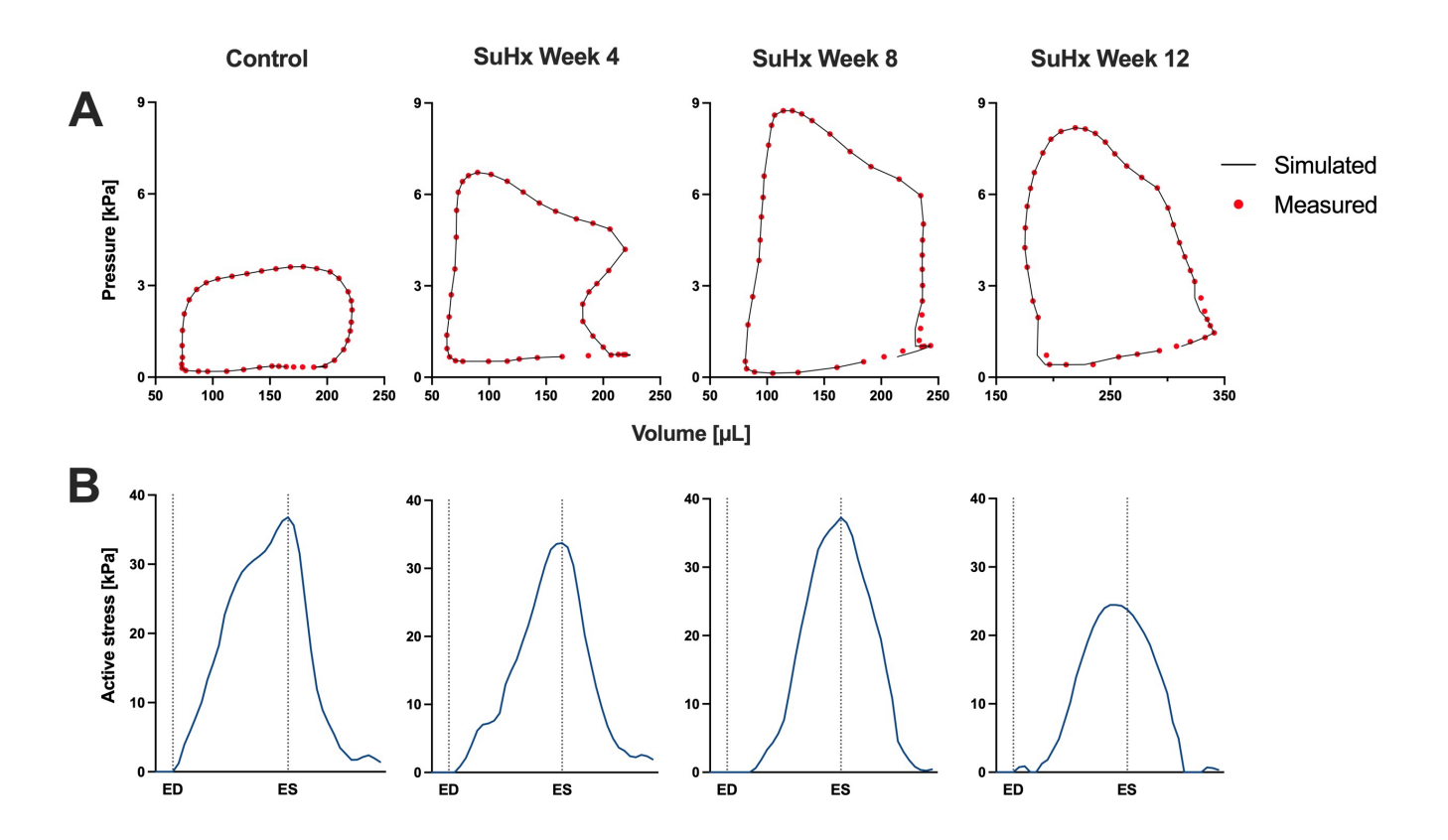


Figure 3. Model calibration results. (**A**) Model-predicted (black lines) and experimental (red circles) RV P-V loops for control, week 4, week 8, and week 12 SuHx cases, demonstrating a good fit between model and data. LV P-V loops are not displayed as the same LV data was used across all cases. (**B**) Time traces of the optimized active stress parameter T_a for each case. On the x-axis we plot the normalized time over one cardiac cycle. The vertical dotted lines indicate the timings of end-diastole (ED) and end-systole (ES). The active stress did not exhibit a distinct trend, likely influenced by specific modeling choices, discussed in Section 4.4.

Our model results reveal a consistent increase in E_{ed} from the control to week 12, while E_{es} demonstrates an upward trend from the control to week 8, followed by a decrease by week 12. This E_{es} trend aligns with the observations by Kwan et al. (2021). However, they observed a decrease in E_{ed} after week 8 which was not evident in our model results.

3.2.2 Myocardial wall stress and strain

Time traces of average Cauchy stress and Green strain in the RVFW along the fiber, circumferential, and apex-to-outflow (AOT) directions are shown in Figure 6 for the different simulated cases. To facilitate the direct comparison of model predicted stress and strain between the different cases, we aligned the pressure-volume (PV) data points within the cardiac cycle in such a way that an equal number of data points were consistently represented from ED to ES for each animal. For this reason, the x-axis in Figure 6 represents normalized time rather than actual time within a cardiac cycle. This approach allowed us to eliminate the expected variations in the timing of ED and ES across the different animals while enhancing the clarity of the comparison between them.

The results indicate that wall stress is highest along the fiber direction and lowest in the AOT direction, in both control and disease cases. At ED and ES, average RVFW stress monotonically increases from control to week 12. However, peak systolic stress, which occurred at the peak systolic pressure, was consistently

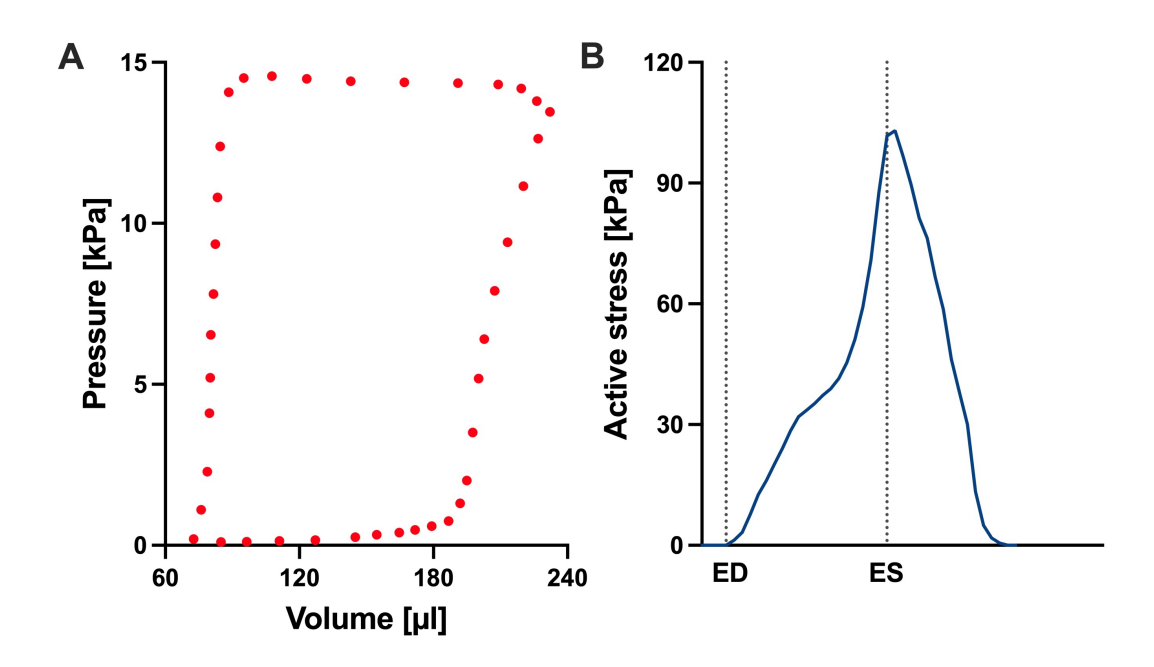


Figure 4. (A) Left ventricular pressure-volume loop used for all simulations in this study. (B) Time trace of the active stress parameter used in the active myocardium model for the left ventricle (LV). On the x-axis we plot the normalized time over one cardiac cycle. The vertical dotted lines indicate the timings of end-diastole (ED) and end-systole (ES). This curve was derived by fitting a biventricular model to left ventricular and right ventricular pressure-volume data from the control animal. The rationale for this approach is that given there are no significant changes to the LV during early-stage PAH, we can assume that the LV material remains at the normal (control) state.

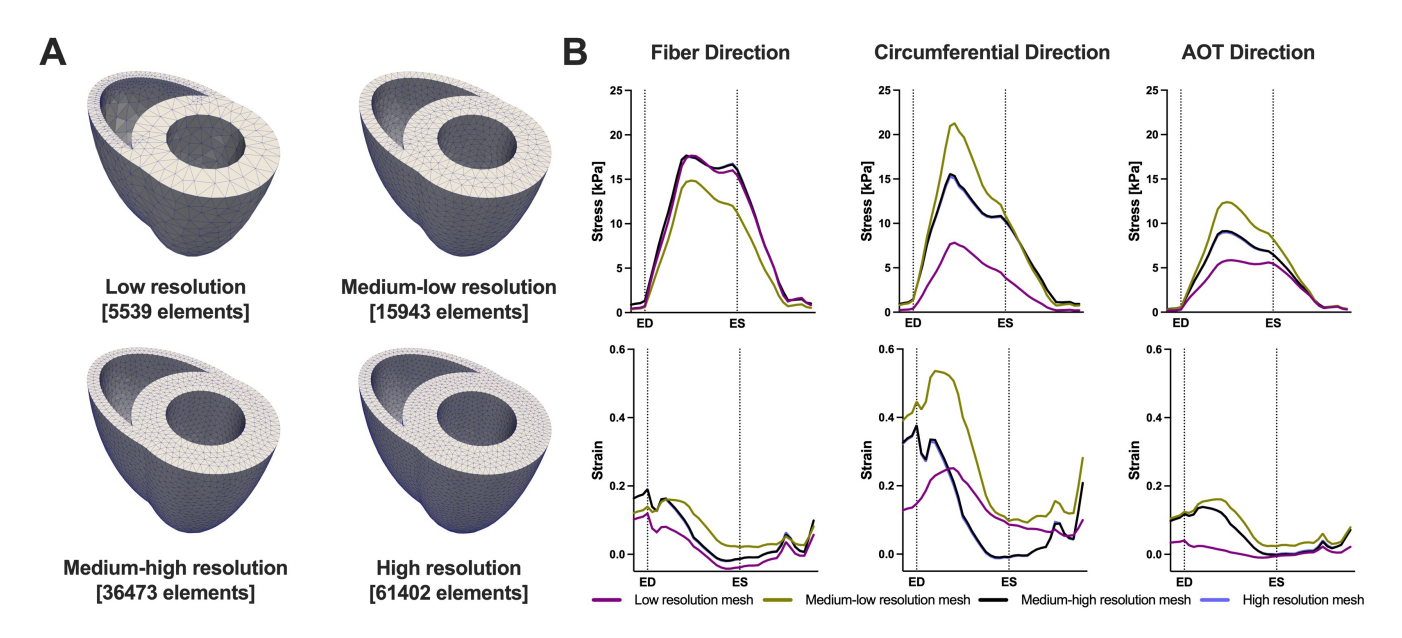


Figure 5. Results of the mesh convergence analysis. (**A**) Four distinct mesh resolutions for the control geometry used in the mesh convergence analysis. (**B**) Model predicted average Cauchy stress and Green strain from the four distinct mesh resolutions. On the x-axis we plot the normalized time over one cardiac cycle. The vertical dotted lines indicate the timings of end-diastole (ED) and end-systole (ES). Model predictions showed low sensitivity to mesh resolution beyond the Medium-high resolution threshold.

higher in control compared to the disease cases except for week 12. In this case, peak systolic fiber stress 222 was comparable with - and even slightly exceeded - that of the control animal (Table 5). This result can be explained by the considerable increase in passive stress at week 12 compared to control, despite a 223 reduced active stress at week 12 (Figure 3B). We note that the total Cauchy stress in (5) is a sum of the passive and active stress components, as defined in (6) and (7) respectively. The passive stress component is heavily influenced by changes in the mechanical properties of the myocardium, such as stiffness. The isotropic stiffness parameter is approximately 2.5 times greater at week 12 compared to control (Table 2). Similarly, in comparison to control, ED pressure and ED volume are about 4 times and 1.75 times greater, respectively, at week 12 (Figure 3A). These changes result in higher wall tension, thus contributing to the elevated passive stress. Hence, these mechanisms combined with our results of ED stress (Table 5), which gives an indication of passive stress and is at least 7.5 times higher in the fiber direction at week 12 compared to control, explain why the peak systolic fiber stress at week 12 is comparable to that at control, 232 despite a diminished active stress at week 12.

On the other hand, variations in wall strain between the control and disease cases were generally less pronounced than the stress variations, but showed an increasing trend with PAH progression at ED and ES, as shown in Table 5. In contrast to peak stresses, peak strains, specifically in the fiber and circumferential directions, were higher in disease compared to control which can be partly explained by the larger RV chamber volumes in the disease cases (Figure 3) leading to larger wall stretching. Peak AOT strain however, stayed within normal (control) values during the 12 week time course of this study.

240 The spatial distribution of stress in the RVFW is also presented in Figure 7, which enables us to observe 241 the transmural variation of RVFW stress at ED and ES. Only small transmural variations in fiber stress 242 were found for the control case. However, the transmural variation of stress becomes more pronounced as PAH progresses - especially at ED - with the endocardial regions consistently experiencing higher stress 243 244 levels compared to epicardial regions.

Effect of geometric and material remodeling on RV mechanics 3.2.3

224

225

226 227

228

229

230

231

233

234

235

236

237

238

239

245

246

247

248

249

250

251

252

253

254 255

256

257

258

259

260

261

262

263

To understand how the RV adapts in PAH, we simulated the effects of changes in pressure with no geometric nor myocardium wall properties changes, with only geometric changes, and with only changes in myocardium wall properties. Geometric changes were based on measured wall thickness (Table 1), while the wall material changes were based on passive and active material parameters fitted to pressure-volume data (Table 2 and Figure 3B). It should be noted that while geometric changes include both increased wall thickness and increased RV radius (as a result of increased ED volume), in this analysis we limited it to increases in wall thickness. Given that the increased chamber radius is generally associated with increased stress, our results indirectly include this effect.

Figure 8 illustrates the three different theoretical cases with varying combinations of remodeling considered in this investigation. The fourth 'full remodeling' case shown in the figure is included here for comparison, as the stress and strain results for this case have been provided previously in Table 5. We also compared the results of these theoretical simulations with the control scenario (Table 5) to provide some context on how these parameter combinations leading to theoretical forms of remodeling impacted RVFW stress and strain.

Our findings (Figure 9) revealed that geometric remodeling in the form of wall thickening plays a crucial role in moderating the increase in fiber stress and strain due to increasing pressure overload in PAH. In the absence of geometric remodeling, RVFW fiber stress and strain significantly increased, even to the level of cases with no remodeling at all. Notably, the addition of geometric remodeling alone had a much greater

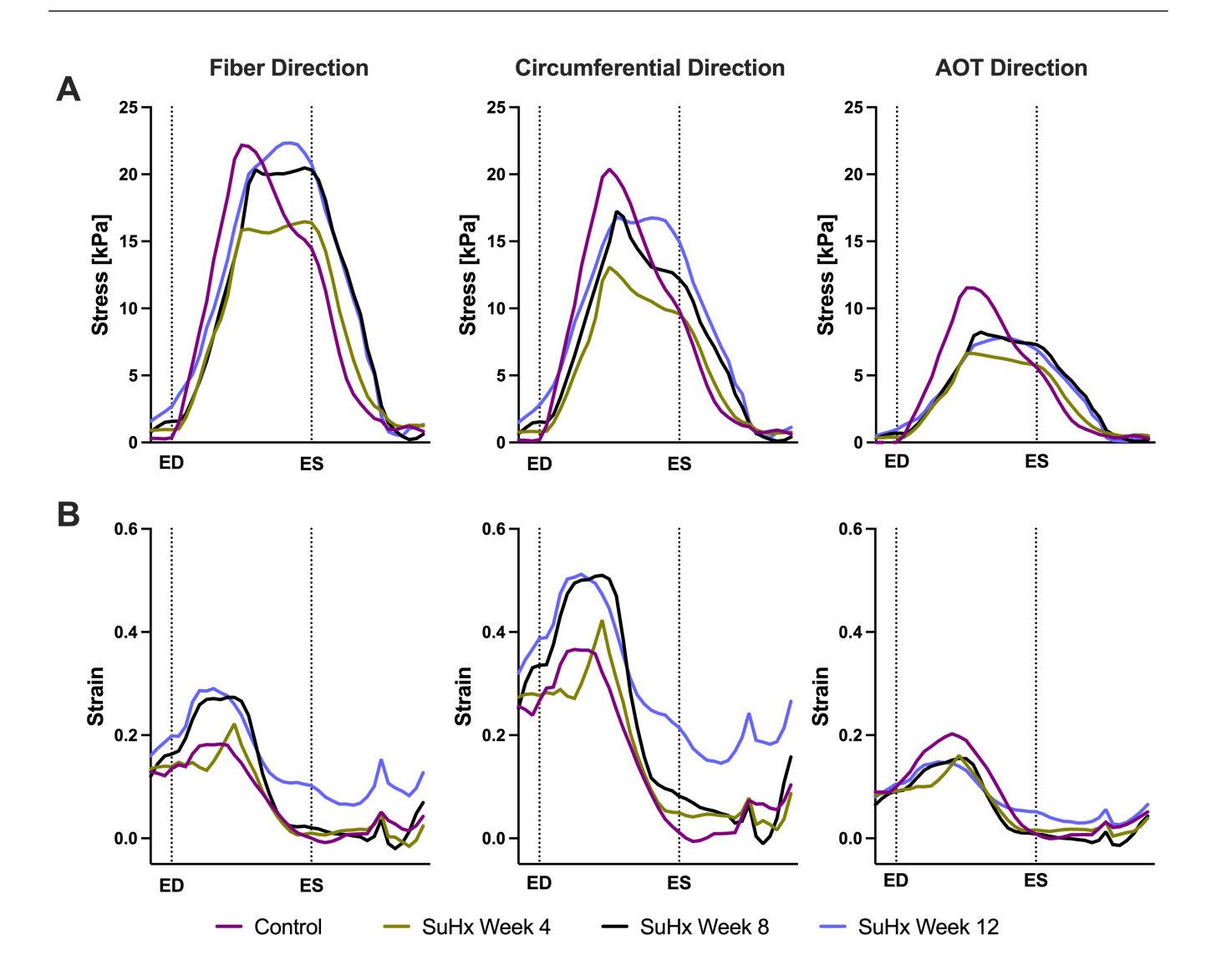


Figure 6. Model predictions of right ventricular free wall stress (**A**) and strain (**B**) in the fiber, circumferential, and apex-to-outflow (AOT) directions for the different cases simulated. On the x-axis we plot the normalized time over one cardiac cycle. The vertical dotted lines indicate the timings of end-diastole (ED) and end-systole (ES). Average stress and strain at ED and ES consistently increased in disease cases compared to the control. However peak systolic stress was higher in control compared to disease, while peak strain showed an opposite trend, being generally higher in disease compared to control.

influence on end-systolic stress compared to end-diastolic stress, because it was almost sufficient to return end-systolic stress to normal. On the other hand, the absence of material remodeling had a much smaller, but not insignificant impact on these metrics, suggesting that the stress and strain response of the RVFW to pressure overload within the 12-week time course of this study is dominated by geometrical remodeling.

4 DISCUSSION

264

265

266

267

268

269

270

271

In this study, we analyzed the right-ventricular mechanical changes due to pulmonary arterial hypertension by incorporating measurements from a sugen-hypoxia rat model into a computational biventricular model. We selected the sugen-hypoxia rat model as it is the smallest animal model to recapitulate vascular lesions resembling those found at autopsy in patients with PAH along with consequent ventricular remodeling

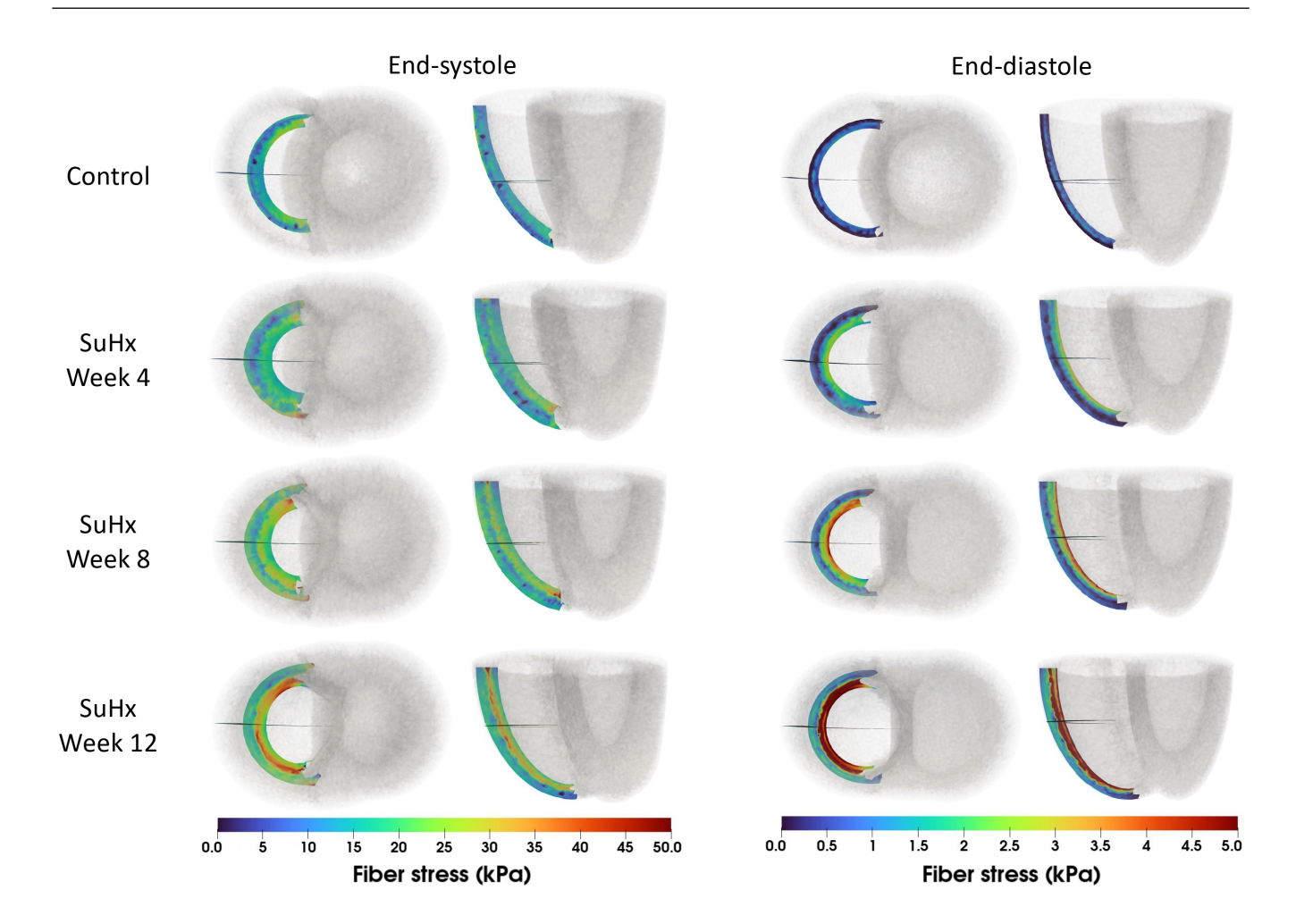


Figure 7. Spatial representation of fiber stress distribution at end-diastole (ED) and end-systole (ES) for the different simulated cases. Shown on axial and lateral slices in the middle of the right ventricular free wall, transmural stress variation increased with PAH progression, consistently higher in endocardial than epicardial regions.

(Taraseviciene-Stewart et al., 2001; Abe et al., 2010; Al-Husseini et al., 2015; Drozd et al., 2017; Jayasekera 272 et al., 2020). The experimental data used in this study included animals up to 12 weeks post-PAH induction, and provided a representative snapshot of different disease stages, including a baseline control case.

273

274

275

276

277

278

279

280

281

282

283

284

285

286

Over the 12-week time course, myocardial stiffness increased by more than 100%, as indicated by end-diastolic elastance. Additionally, myocardial contractility, indexed by end-systolic elastance, almost doubled by week 8 compared to control, which was then followed by a decrease to within the baseline range by week 12.

Both end-diastolic and end-systolic stress and strain in the fiber, circumferential and apex-to-outflow directions consistently increased with disease progression; peak strain within the cardiac cycle exhibited a similar increase, except in the peak apex-to-outflow strain which remained within baseline limits. A contrasting trend was observed in peak systolic stress, occurring at the peak systolic pressure time point within the cardiac cycle. Our findings indicated that peak systolic stress was consistently higher in the control case, except for the peak systolic fiber stress at week 12, which marginally exceeded control. Overall, transmural stress variation across the RVFW was notably more pronounced in disease, with endocardial regions experiencing higher stress levels compared to epicardial regions of the RVFW.

Control Control No remodeling Only material remodeling SuHx Only geometric remodeling Full remodeling

Figure 8. The set of simulations used to study the effect of geometric and material remodeling on RV mechanics by combining optimized material parameters and mesh geometries from control and SuHx (sugen-hypoxia) cases. Three theoretical combinations were considered: 'no remodeling' (control mesh & control material), 'only material remodeling' (control mesh & SuHx material) and 'only geometric remodeling' (SuHx mesh & control material). For all combinations, the geometric remodeling was quantified by the measured wall thickness (Table 1), the material remodeling by the optimized passive and active material parameters (Table 2 and Figure 3B), while the hemodynamic data was fixed to that of the disease case in question. The 'full remodeling' case (SuHx mesh & SuHx material) is only added for comparison and results for this simulation have been presented previously in Table 5.

Finally, we analyzed the relative effects of geometric and material remodeling on RV mechanics indexed by wall stress and strain. The simulations indicated that changes in heart geometry, particularly through wall thickening, had a more pronounced impact on moderating wall stress and strain than did changes in the material properties, such as wall stiffness. Notably, the influence of wall stiffening was pronounced at end-diastole, suggesting that the effect of the significant increase in myocardial stiffness on RVFW stress and strain was not negligible. Still, over the 12-week time course of this study, our results suggest that the stress and strain response of the RV was dominated by wall thickening.

4.1 Ventricular stiffness and contractility

End-diastolic elastance (E_{ed}) and end-systolic elastance (E_{es}) serve as valuable indices for evaluating ventricular stiffness and contractility, respectively (Templeton et al., 1972; Suga and Sagawa, 1974). The gold standard for computing these metrics is by transiently varying RV preload, generating multi-beat pressure-volume loops subsequently used for E_{ed} and E_{es} measurements (Suga et al., 1973; Maughan et al., 1979). This method, while also applied in clinical studies (Dell'Italia and Walsh, 1988; Hsu et al., 2020), is less established in the clinical setting compared to experimental studies. Here, we implemented a different approach that is comparable to the gold standard. We altered RV loading conditions by perturbing end-diastolic and end-systolic pressure, keeping all other parameters fixed. We then computed E_{ed} and E_{es} as the slope of the resulting pressure-volume relationship, i.e., $\Delta P/\Delta V$. This approach has been used previously for calculating E_{es} (Finsberg et al., 2018a,b). We observed that the model predicts a slight increase in diastolic stiffness from week 8 to week 12, although the material stiffness parameter displayed in Table 2 is reduced. This apparent inconsistency is most likely the result of the increased wall thickness at week 12, which directly impacts the overall chamber elastance.

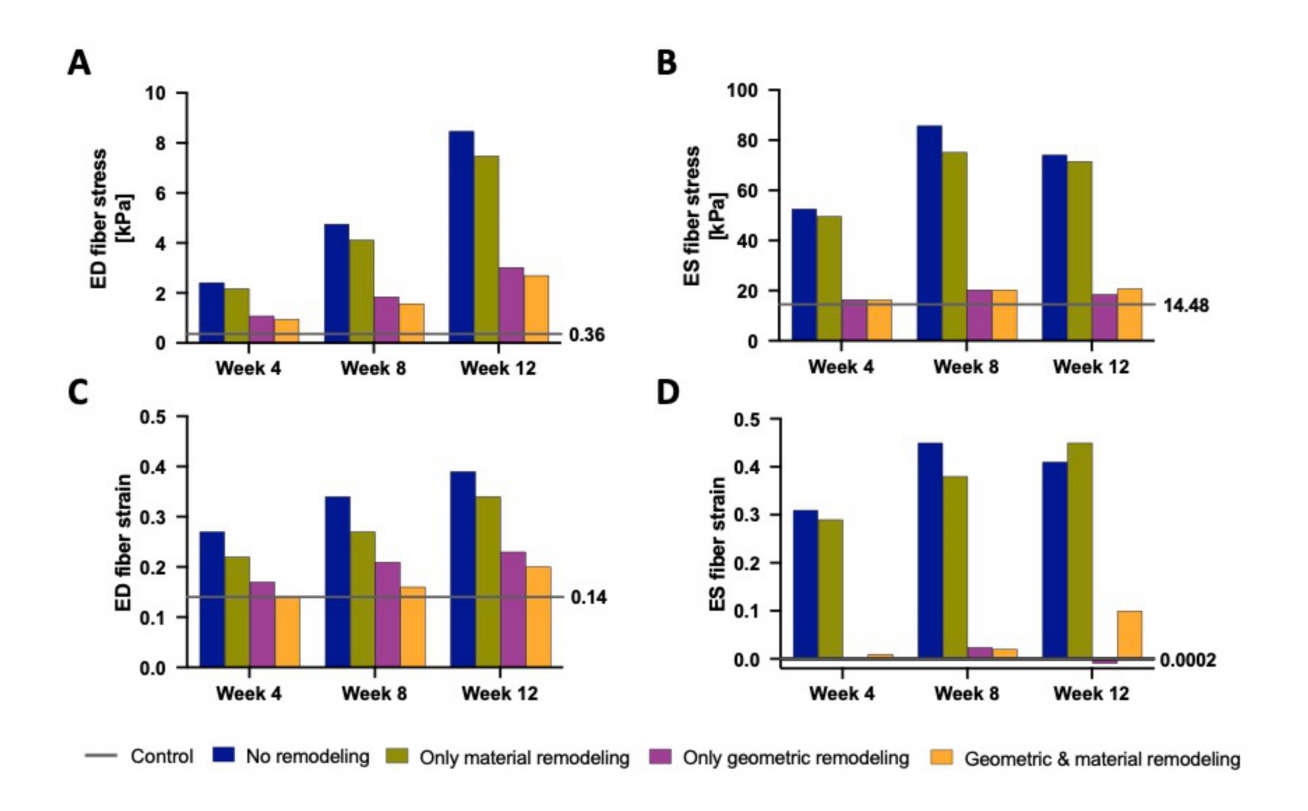


Figure 9. End-diastolic fiber stress (**A**), End-systolic fiber stress (**B**), End-diastolic fiber strain (**C**) and End-systolic fiber strain (**D**) at 4 weeks to 12 weeks post-PAH induction when considering no remodeling (blue bars), only material remodeling (green bars) and only geometric remodeling (purple bars). For reference, the corresponding stress and strain values for the fully remodeled cases (orange bars) and for the control case (gray lines) are plotted. The control values are also called out to the right-hand side of each plot.

Nevertheless, the general trend of elevated stiffness in disease compared to control aligns with previous measurements in sugen-hypoxia (Kwan et al., 2021), monocrotaline (Vélez-Rendón et al., 2018), and pulmonary artery banding (Rain et al., 2016) animal models of PAH. Table 4 displays results from the study by Kwan et al. (2021), supporting this general trend. Likewise, Rain et al. (2016) demonstrated increased RV stiffness in rats with mild and severe RV dysfunction, attributing the rise in mild dysfunction to myofibril-mediated stiffness and in severe dysfunction to both increased myofibril stiffness and fibrosis. In a monocrotaline rat model, Vélez-Rendón et al. (2018) reported stiffening of the passive myocardium after 4 weeks post-PAH induction, observing an initial decrease in stiffness at week 1, possibly due to a temporary increase in myocardial compliance required to preserve RV stroke volume. However, by 2 weeks post-PAH induction, passive stiffness began trending upward. Our results also align with human clinical (Rain et al., 2013; Trip et al., 2015; Hsu et al., 2018) and computational (Finsberg et al., 2019) studies of PAH. In all four studies, they noted a progressive increase in RV passive stiffness in PAH patients compared to controls. This increase was found to be influenced by the degree of remodeling or the severity of the disease.

In our study, we observed an initial twofold increase in contractility from control to week 8, followed by a decrease at week 12, indicating a down-regulation of RV contractility by 12 weeks post-PAH induction. This initial increase in contractility, reported in both animal (Blaudszun and Morel, 2012; Vélez-Rendón et al., 2018; Kwan et al., 2021) and human (Rain et al., 2013; Hsu et al., 2018; Finsberg et al., 2019) PAH studies, is linked to adaptive hypertrophy (Bogaard et al., 2009; Kwan et al., 2021), believed to preserve

systolic function in early PAH stages (Naeije et al., 2014; Naeije and Manes, 2014). However, increased ventricular contractility is unsustainable, and a down-regulation of contractile force is commonly observed as the disease progresses (Fan et al., 1997; Bogaard et al., 2009). Our model results indicate that this down-regulation starts after 8 weeks post-PAH induction in a SuHx-rat model. Few PAH studies have explored the time course of contractility changes; most only distinguish between control and PAH subjects. In a relevant study, Finsberg et al. (2019) noted a 20% initial increase in RV contractility in mild RV remodeling, later down-regulating in severely remodeled cases to values below the control. Their study, focusing on human subjects, did not specify the time-course of the significant decrease in contractility but distinguished between mild and severe remodeling based on RV end-diastolic volume to LV end-diastolic volume ratios. Similarly, Kwan et al. (2021) reported down-regulation at 10 weeks post-PAH induction in a sugen-hypoxia animal model, with values still higher than control at the 10-week timepoint. This suggests a peak in RV contractility at 8 weeks post-PAH induction, followed by a progressive down-regulation, aligning with our observations.

4.2 Myocardial wall stress

Ventricular wall stress, particularly at end-systole (ES) and end-diastole (ED), plays a pivotal role in systolic and diastolic cardiac function. Its significant correlation with myocardial oxygen consumption and adverse cardiac remodeling has been well-established by previous studies (Strauer, 1979; Bogaard et al., 2009; Alter et al., 2016; Haque and Wang, 2017). Pressure overload directly impacts wall stress, adhering to the law of Laplace, and an elevation in wall stress can hinder myocardial oxygen supply by compressing coronary circulation (Chin et al., 2005). Consequently, deviations from normal or baseline wall stress can detrimentally affect oxygen availability to cardiomyocytes, potentially leading to cardiac ischemia, adverse remodeling, and ultimately, heart failure.

The inverse linear correlation identified by Quaife et al. (2006) between ES wall stress and RV ejection fraction, supported by Alter et al. (2016) for the LV, emphasizes the critical relationship between wall stress and cardiac function. This underscores the potential of wall stress as a diagnostic index for evaluating heart performance in disease. However, the lack of a direct method to measure RV wall stress necessitates reliance on mathematical approximations, with several proposed methods in the literature and no universally recognized gold standard. Consequently, the accuracy and agreement of these approximations carry significant experimental and clinical implications.

Our model results demonstrate a progressive increase in ED and ES fiber stress in disease compared to control. Circumferential and apex-to-outflow stress also exhibit an increase at ED and ES. Comparison with existing literature that reported wall stress in PAH, consistently revealed increased RV wall stress at ED and ES in disease compared to control (Quaife et al., 2006; Vélez-Rendón et al., 2018; Gold et al., 2020; Kwan et al., 2021), despite variations in geometric model assumptions and stress computation methods across these studies. Vélez-Rendón et al. (2018) and Kwan et al. (2021) assumed a spherical RV geometry and used the thin-walled Laplace law to estimate fiber stress in the RV free wall. Quaife et al. (2006) also assumed a spherical RV but employed a modified Laplace law suitable for non-circular cross-sections (Janz et al., 1989). Gold et al. (2020) utilized a two-dimensional model based on short-axis echo images and estimated wall stress using the von Mises formula, providing an equivalent stress over the entire RV rather than individual stress components. Finsberg et al. (2019), utilizing a modeling technique and stress approximation method similar to our study, did not report ED and ES wall stress, but instead reported peak fiber stress, which does not necessarily coincide with end-diastole or end-systole. Interestingly, they reported an increase in peak fiber stress only in severely remodeled cases which they defined as a ratio

of RV ED volume (RVEDV) to LV ED volume (LVEDV) greater than 1.5. In the mildly remodeled case 371 (RVEDV/LVEDV < 1.5), peak fiber stress was at control level. This finding aligns with our observation that peak fiber stress, which occured at a time point between ED and ES in our model, only surpassed 372 control values at 12 weeks post-PAH induction, although it exhibited an increasing trend in the disease 373 374 cases (Figure 6). This suggests that peak fiber stress increases as PAH progresses, and RV geometric remodeling transitions from wall thickening to dilation.

Effect of geometric and material remodeling

375

376

377

378

379

380

381

382

383

384

385

386

387

388

389

390

391

392

393 394

395

396 397

398

399

400

At the onset of PAH, both geometric and material remodeling occur simultaneously, and manifest as compensatory mechanisms. Our study aimed to isolate these remodeling mechanisms and explore their individual impacts on RV mechanics, as indexed by wall stress and strain. The results revealed that material remodeling has a minimal effect on wall stress and strain, while geometric remodeling plays a predominant role in reducing these parameters as the disease progresses. This agrees with existing knowledge that attributes the primary role of geometric remodeling to the reduction of wall stress (to normal physiological values) in the presence of pressure overload (Grossman et al., 1975).

Our study provides quantifiable insights into these established findings. Specifically, we found that if the RV wall had not thickened, ED fiber stress would have exhibited a substantial increase, reaching six-fold by week 4, eleven-fold by week 8, and a remarkable twenty-fold increase by week 12 compared to baseline (control) levels. However, due to observed geometric remodeling, the maximum increase in ED wall stress was limited to seven-fold, occurring at week 12. Similarly, ES wall stress would have experienced a three-fold increase by week 4 and a five-fold increase at weeks 8 and 12 without RV wall thickening. Again, the presence of RV wall thickening significantly mitigated these increases, with ES wall stress nearly fully normalized by week 12.

From these findings, two key takeaways emerge. Firstly, while geometric remodeling alone fell short of fully normalizing wall stress in the 12 week time course of this study, it effectively mitigated the majority of stress increases associated with rising RV afterload. Secondly, the presented magnitudes of wall stress increase, in the absence of RV thickening, shed light on what can be expected when RV geometric remodeling transitions from wall thickening to wall thinning in the later stages of PAH (in an attempt to maintain stroke volume and cardiac output). These excessive wall stress levels may lead to a detrimental sequence of cardiac ischemia, further compromised RV contractility, causing additional RV dilation, and ultimately culminating in RV dysfunction.

Limitations and future research directions 4.4

There are a number of important limitations to the present study, which should motivate further 401 experimental and computational research. We applied the computational framework to a limited cohort 402 of four animals, which included one normotensive and three hypertensive animals at distinct time points. 403 Although the animals chosen for this study were representative of the control and disease groups, they do 404 not represent a full description of the longitudinal and progressive remodeling of the RV in PAH. While 405 not comprehensive, the study aimed to analyze mechanical changes in the RV during the initial 12 weeks 406 post-PAH induction. Future research could apply the framework to a larger cohort over an extended period 407 for a better understanding of RV behavior in PAH progression. 408

We only fit a single passive material parameter, while the others are set to values from the literature. This 409 modeling decision was necessitated by the limited data available for the optimization. Attempting to fit all 410 four parameters in (3) to in vivo P-V data would have substantially increased the computational cost. More 411

importantly, it would have resulted in a scenario where multiple sets of parameters would minimized the 412 413 cost function (8), rendering the chosen optimal parameter set overly sensitive to the initial guess provided to the optimization algorithm. While our approach aligns with previous research suggesting that a unique 414 415 solution can be achieved by optimizing a single parameter (or at most two of the parameters) of (3) when 416 fitting to in vivo P-V data (Hadjicharalambous et al., 2015; Balaban et al., 2017), it is crucial to recognize its inherent limitations, specifically the dependence on parameter values sourced from the literature. More 417 418 detailed experimental data, for example local ventricular strains estimated from magnetic resonance images, 419 or biaxial stress-strain data extracted from myocardial tissue mechanical testing will be important for more 420 accurate characterization of material properties, as well as for validation of the model results. As shown in Figure 3, the passive filling phase - which is the part used for optimizing a_{RV} - is nearly flat for several of 421 the P-V loops used in this study. As such, small deviations in the pressure can lead to large variations in the 422 423 fitted parameters. In addition, our decision to fit the isotropic material parameter in 3, while keeping the parameter that describes stiffness in the fiber direction, a_f , constant in both control and disease cases, may 424 have contributed to the absence of a discernible trend in active stress development, as depicted in Figure 425 3B. To address these issues, future model development should be based on more comprehensive datasets 426 which should enable improved characterization of the passive tissue stiffness. 427

Due to the unavailability of imaging data of sufficient resolution to build meshes for the rats used in this study, we employed idealized biventricular geometries in the mechanical model. Despite this limitation, the idealized geometry gives insights on the effect of wall thickening on RV mechanics with PAH progression. It is important to note that the altered septal wall positions depicted in Figure 1 as the disease progresses stems from the methodology used in generating the biventricular meshes. Specifically, it is a result of the inflation of the mesh geometries to match the initial cavity volumes outlined in Table 1. While the magnitude of septal wall flattening was not validated against imaging data, qualitatively, it is consistent with cardiac magnetic resonance imaging data obtained from a different rat at time points similar to those used in this study.

428

429

430

431

432

433

434

435 436

437 We modeled the myocardium as transversely isotropic. The passive myocardium is inherently complex, displaying strong non-linearity and anisotropy, and would require an orthotropic model to fully characterize 438 its mechanical behavior. However, it has been documented that a transversely isotropic formulation of the 439 440 Holzapfel-Ogden law strikes a good balance between parameter identifiability – the ability to determine a unique parameter set given limited amount and quality of the data – and model fidelity – the ability of the 441 model to adequately represent cardiac deformation and function (Hadjicharalambous et al., 2015; Gjerald 442 443 et al., 2015). Given that the data available for model fitting in this study was quite limited, and the extensive use of a transversely isotropic model to approximate orthotropic cardiac tissue properties in the literature 444 (Guccione et al., 1991; Xi et al., 2011; Balaban et al., 2017; Finsberg et al., 2018b; Avazmohammadi et al., 445 2019), we deemed the use of this model to be appropriate. 446

447 We did not include rat-specific measurements of fiber orientation or regional strain. Instead, we implemented the same fiber orientation across all simulations using a rule-based method and assumed 448 a transmural variation in the fiber direction. This modeling choice is a candidate for further refinement 449 450 as some studies have reported changes in myofiber architecture in PH (Avazmohammadi et al., 2017; 451 Mendiola et al., 2023). However, it remains unclear to what degree myofiber angle remodeling occurs and whether previous studies are confounded by the animal model, or the stage of disease. In addition, our 452 assumption of transmural (through-thickness) variation in the fiber direction is a common assumption in 453 454 computational studies of cardiac mechanics that employ a rule-based method to assign myocardial fibers to the mesh geometry and has been validated by histology (Streeter Jr et al., 1969; Hill et al., 2014) and 455

- 456 DTI-based studies (Hsu et al., 1998; Holmes et al., 2000; Scollan et al., 2000) of cardiac fiber architecture.
- 457 Nevertheless, future research could benefit from incorporating diffusion tensor magnetic resonance imaging
- 458 (DT-MRI) data from Sprague-Dawley rats to create a more accurate representation of the fiber architecture.
- 459 Finally, while isoflurane and other anesthetics can alter cardiovascular function (Loushin, 2005), isoflurane
- 460 was carefully regulated at 2% (in 100% O₂), below reported doses that drastically alter heart rate and
- 461 hemodynamics (Yang et al., 2014; Pang et al., 2018). The effects on hemodynamics due to isoflurane were
- 462 likely small compared with the differences due to the PAH treatment, as seen previously (Hill et al., 2014;
- 463 Vélez-Rendón et al., 2019; Kwan et al., 2021).

5 CONCLUSION

- 464 The combination of finite element modeling and experimental measurements of hemodynamics reveals
- 465 significant mechanical changes associated with a moderately changed functional state, as indicated by
- 466 changes in ejection fraction. In this analysis we find that increased RV wall thickness, myocardial
- 467 contractility and stiffness are compensatory in the initial 12 weeks post-disease induction, and these
- 468 mechanisms work to alleviate the increase in wall stress and strain due to pressure overload. In the absence
- 469 of these remodeling mechanisms, our model predicted that wall stress would have increased more than
- 470 twenty-fold from baseline levels, which could have serious implications for myocardial perfusion and,
- 471 subsequently, cardiac function.

CONFLICT OF INTEREST STATEMENT

- 472 The authors declare that the research was conducted in the absence of any commercial or financial
- 473 relationships that could be construed as a potential conflict of interest.

AUTHOR CONTRIBUTIONS

- 474 The Author Contributions section is mandatory for all articles, including articles by sole authors. If an
- 475 appropriate statement is not provided on submission, a standard one will be inserted during the production
- 476 process. The Author Contributions statement must describe the contributions of individual authors referred
- 477 to by their initials and, in doing so, all authors agree to be accountable for the content of the work. Please
- 478 see here for full authorship criteria.

FUNDING

- 479 This research was supported by the US National Heart, Lung, and Blood Institute Grants 1R25HL145817-
- 480 01 & 1R01HL155945-01, the US National Science Foundation CAREER Award 2046259, The Research
- 481 Council of Norway through Grant 316185, and the Simula-UCSD-University of Oslo Research and PhD
- 482 training (SUURPh).

ACKNOWLEDGMENTS

- 483 The research presented in this paper has benefited from the Experimental Infrastructure for Exploration
- 484 of Exascale Computing (eX3), which is financially supported by the Research Council of Norway under

485 contract 270053.

SUPPLEMENTAL DATA

- 486 Supplementary Material should be uploaded separately on submission, if there are Supplementary Figures,
- 487 please include the caption in the same file as the figure. LaTeX Supplementary Material templates can be
- 488 found in the Frontiers LaTeX folder.

DATA AVAILABILITY STATEMENT

- 489 The data and code employed in this study have been publicly deposited on Github at https://github.
- 490 com/oscarodeigah/rv_pah_project to facilitate replication and further investigation.

REFERENCES

- 491 Abe, K., Toba, M., Alzoubi, A., Ito, M., Fagan, K. A., Cool, C. D., et al. (2010). Formation of plexiform
- lesions in experimental severe pulmonary arterial hypertension. *Circulation* 121, 2747–2754
- 493 Al-Husseini, A., Wijesinghe, D. S., Farkas, L., Kraskauskas, D., Drake, J. I., Van Tassel, B., et al. (2015).
- Increased eicosanoid levels in the sugen/chronic hypoxia model of severe pulmonary hypertension. *PLoS*
- 495 *One* 10, e0120157
- 496 Alter, P., Koczulla, A. R., Nell, C., Figiel, J. H., Vogelmeier, C. F., and Rominger, M. B. (2016). Wall
- 497 stress determines systolic and diastolic function—characteristics of heart failure. *International journal*
- 498 *of cardiology* 202, 685–693
- 499 Avazmohammadi, R., Hill, M., Simon, M., and Sacks, M. (2017). Transmural remodeling of right
- ventricular myocardium in response to pulmonary arterial hypertension. APL bioengineering 1
- 501 Avazmohammadi, R., Mendiola, E. A., Soares, J. S., Li, D. S., Chen, Z., Merchant, S., et al. (2019). A
- computational cardiac model for the adaptation to pulmonary arterial hypertension in the rat. *Annals of*
- *biomedical engineering* 47, 138–153
- 504 Badagliacca, R., Poscia, R., Pezzuto, B., Nocioni, M., Mezzapesa, M., Francone, M., et al. (2015).
- Right ventricular remodeling in idiopathic pulmonary arterial hypertension: adaptive versus maladaptive
- morphology. *The Journal of Heart and Lung Transplantation* 34, 395–403
- 507 Balaban, G., Finsberg, H., Odland, H. H., Rognes, M. E., Ross, S., Sundnes, J., et al. (2017). High-
- resolution data assimilation of cardiac mechanics applied to a dyssynchronous ventricle. *International*
- journal for numerical methods in biomedical engineering 33, e2863
- 510 Bayer, J. D., Blake, R. C., Plank, G., and Trayanova, N. A. (2012). A novel rule-based algorithm for
- assigning myocardial fiber orientation to computational heart models. *Annals of biomedical engineering*
- 512 40, 2243–2254
- 513 Blaudszun, G. and Morel, D. R. (2012). Superiority of desflurane over sevoflurane and isoflurane in the
- presence of pressure-overload right ventricle hypertrophy in rats. The Journal of the American Society of
- 515 *Anesthesiologists* 117, 1051–1061
- 516 Bogaard, H. J., Abe, K., Noordegraaf, A. V., and Voelkel, N. F. (2009). The right ventricle under
- pressure: cellular and molecular mechanisms of right-heart failure in pulmonary hypertension. *Chest*
- 518 135, 794–804
- 519 Broyden, C. G. (1970). The convergence of a class of double-rank minimization algorithms 1. general
- 520 considerations. *IMA Journal of Applied Mathematics* 6, 76–90
- 521 Chin, K. M., Kim, N. H., and Rubin, L. J. (2005). The right ventricle in pulmonary hypertension. *Coronary*
- 522 *artery disease* 16, 13–18

Dell'Italia, L. J. and Walsh, R. A. (1988). Application of a time varying elastance model to right ventricular performance in man. *Cardiovascular research* 22, 864–874

- 525 Drozd, K., Ahmadi, A., Deng, Y., Jiang, B., Petryk, J., Thorn, S., et al. (2017). Effects of an endothelin
- 526 receptor antagonist, macitentan, on right ventricular substrate utilization and function in a sugen
- 527 5416/hypoxia rat model of severe pulmonary arterial hypertension. *Journal of Nuclear Cardiology* 24,
- 528 1979–1989
- Fan, D., Wannenburg, T., and de Tombe, P. P. (1997). Decreased myocyte tension development and calcium responsiveness in rat right ventricular pressure overload. *Circulation* 95, 2312–2317
- 531 Finsberg, H., Balaban, G., Ross, S., Håland, T. F., Odland, H. H., Sundnes, J., et al. (2018a). Estimating
- cardiac contraction through high resolution data assimilation of a personalized mechanical model.
- 533 *Journal of computational science* 24, 85–90
- 534 Finsberg, H., Xi, C., Tan, J. L., Zhong, L., Genet, M., Sundnes, J., et al. (2018b). Efficient estimation of
- 535 personalized biventricular mechanical function employing gradient-based optimization. *International*
- journal for numerical methods in biomedical engineering 34, e2982
- 537 Finsberg, H., Xi, C., Zhao, X., Tan, J. L., Genet, M., Sundnes, J., et al. (2019). Computational quantification
- of patient-specific changes in ventricular dynamics associated with pulmonary hypertension. *American*
- *Journal of Physiology-Heart and Circulatory Physiology* 317, H1363–H1375
- 540 Finsberg, H. N. T. (2019). pulse: A python package based on fenics for solving problems in cardiac
- mechanics. *Journal of Open Source Software* 4, 1539
- 542 Fletcher, R. (1970). A new approach to variable metric algorithms. *The computer journal* 13, 317–322
- 543 Geuzaine, C. and Remacle, J.-F. (2009). Gmsh: A 3-d finite element mesh generator with built-in pre-and
- post-processing facilities. *International journal for numerical methods in engineering* 79, 1309–1331
- 545 Gjerald, S., Hake, J., Pezzuto, S., Sundnes, J., and Wall, S. T. (2015). Patient–specific parameter estimation
- for a transversely isotropic active strain model of left ventricular mechanics. In *Statistical Atlases and*
- 547 Computational Models of the Heart-Imaging and Modelling Challenges: 5th International Workshop,
- 548 STACOM 2014, Held in Conjunction with MICCAI 2014, Boston, MA, USA, September 18, 2014, Revised
- 549 Selected Papers 5 (Springer), 93–104
- 550 Gold, J., Akazawa, Y., Sun, M., Hunter, K. S., and Friedberg, M. K. (2020). Relation between right
- ventricular wall stress, fibrosis, and function in right ventricular pressure loading. *American Journal of*
- 552 *Physiology-Heart and Circulatory Physiology* 318, H366–H377
- 553 Goldfarb, D. (1970). A family of variable-metric methods derived by variational means. *Mathematics of*
- 554 *computation* 24, 23–26
- 555 Grossman, W., Jones, D., McLaurin, L. P., et al. (1975). Wall stress and patterns of hypertrophy in the
- 556 human left ventricle. *The Journal of clinical investigation* 56, 56–64
- 557 Guccione, J. M., McCulloch, A. D., and Waldman, L. (1991). Passive material properties of intact
- ventricular myocardium determined from a cylindrical model
- 559 Hadjicharalambous, M., Chabiniok, R., Asner, L., Sammut, E., Wong, J., Carr-White, G., et al. (2015).
- Analysis of passive cardiac constitutive laws for parameter estimation using 3d tagged mri. *Biomechanics*
- and modeling in mechanobiology 14, 807–828
- 562 Haque, Z. K. and Wang, D.-Z. (2017). How cardiomyocytes sense pathophysiological stresses for cardiac
- remodeling. *Cellular and Molecular Life Sciences* 74, 983–1000
- 564 Hill, M. R., Simon, M. A., Valdez-Jasso, D., Zhang, W., Champion, H. C., and Sacks, M. S. (2014).
- Structural and mechanical adaptations of right ventricle free wall myocardium to pressure overload.
- 566 Annals of biomedical engineering 42, 2451–2465

567 Holmes, A. A., Scollan, D., and Winslow, R. L. (2000). Direct histological validation of diffusion tensor

- mri in formaldehyde-fixed myocardium. Magnetic Resonance in Medicine: An Official Journal of the
- International Society for Magnetic Resonance in Medicine 44, 157–161
- 570 Holzapfel, G. A. and Ogden, R. W. (2009). Constitutive modelling of passive myocardium: a structurally
- 571 based framework for material characterization. *Philosophical Transactions of the Royal Society A:*
- 572 *Mathematical, Physical and Engineering Sciences* 367, 3445–3475
- Hood, P. and Taylor, C. (1974). Navier-stokes equations using mixed interpolation. *Finite element methods* in flow problems, 121–132
- Howard, L. (2011). Prognostic factors in pulmonary arterial hypertension: assessing the course of the disease. *European Respiratory Review* 20, 236–242
- 577 Hsu, E. W., Muzikant, A., Matulevicius, S., Penland, R., and Henriquez, C. (1998). Magnetic
- resonance myocardial fiber-orientation mapping with direct histological correlation. *American Journal*
- of Physiology-Heart and Circulatory Physiology 274, H1627–H1634
- 580 Hsu, S., Kokkonen-Simon, K. M., Kirk, J. A., Kolb, T. M., Damico, R. L., Mathai, S. C., et al. (2018).
- Right ventricular myofilament functional differences in humans with systemic sclerosis-associated
- versus idiopathic pulmonary arterial hypertension. *Circulation* 137, 2360–2370
- 583 Hsu, S., Simpson, C. E., Houston, B. A., Wand, A., Sato, T., Kolb, T. M., et al. (2020). Multi-beat right
- ventricular-arterial coupling predicts clinical worsening in pulmonary arterial hypertension. *Journal of*
- *the American Heart Association* 9, e016031
- 586 Hurdman, J., Condliffe, R., Elliot, C., Davies, C., Hill, C., Wild, J., et al. (2012). Aspire registry: assessing
- the spectrum of pulmonary hypertension identified at a referral centre. *European Respiratory Journal*
- 588 39, 945–955
- 589 Janz, R., Ozpetek, S., Ginzton, L., and Laks, M. (1989). Regional stress in a noncircular cylinder.
- 590 Biophysical Journal 55, 173–182
- 591 Jayasekera, G., Wilson, K. S., Buist, H., Woodward, R., Uckan, A., Hughes, C., et al. (2020). Understanding
- longitudinal biventricular structural and functional changes in a pulmonary hypertension sugen-hypoxia
- rat model by cardiac magnetic resonance imaging. *Pulmonary Circulation* 10, 2045894019897513
- 594 Kakaletsis, S., Malinowski, M., Snider, J. C., Mathur, M., Sugerman, G. P., Luci, J. J., et al. (2023).
- 595 Untangling the mechanisms of pulmonary arterial hypertension-induced right ventricular stiffening in a
- large animal model. *Acta Biomaterialia* 171, 155–165
- 597 Kwan, E. D., Vélez-Rendón, D., Zhang, X., Mu, H., Patel, M., Pursell, E., et al. (2021). Distinct time
- courses and mechanics of right ventricular hypertrophy and diastolic stiffening in a male rat model of
- 599 pulmonary arterial hypertension. American Journal of Physiology-Heart and Circulatory Physiology
- 600 321, H702–H715
- 601 Lamberts, R. R., Vaessen, R. J., Westerhof, N., and Stienen, G. J. (2007). Right ventricular hypertrophy
- causes impairment of left ventricular diastolic function in the rat. Basic research in cardiology 102,
- 603 19–27
- 604 Lin, D. and Yin, F. (1998). A multiaxial constitutive law for mammalian left ventricular myocardium in
- steady-state barium contracture or tetanus. Journal of biomechanical engineering 120, 504–517
- Logg, A., Mardal, K.-A., and Wells, G. (2012). *Automated solution of differential equations by the finite element method: The FEniCS book*, vol. 84 (Springer Science & Business Media)
- 608 Loushin, M. K. (2005). The effects of anesthetic agents on cardiac function. *Handbook of cardiac anatomy,*609 *physiology, and devices*, 171–180
- 610 Maughan, W. L., Shoukas, A. A., Sagawa, K., and Weisfeldt, M. L. (1979). Instantaneous pressure-volume
- relationship of the canine right ventricle. *Circulation research* 44, 309–315

612 Mendiola, E. A., da Silva Gonçalves Bos, D., Leichter, D. M., Vang, A., Zhang, P., Leary, O. P., et al.

- 613 (2023). Right ventricular architectural remodeling and functional adaptation in pulmonary hypertension.
- 614 *Circulation: Heart Failure* 16, e009768
- 615 Meyer, P., Filippatos, G. S., Ahmed, M. I., Iskandrian, A. E., Bittner, V., Perry, G. J., et al. (2010). Effects
- of right ventricular ejection fraction on outcomes in chronic systolic heart failure. *Circulation* 121,
- 617 252–258
- 618 Naeije, R., Brimioulle, S., and Dewachter, L. (2014). Biomechanics of the right ventricle in health and
- disease (2013 grover conference series). *Pulmonary circulation* 4, 395–406
- 620 Naeije, R. and Manes, A. (2014). The right ventricle in pulmonary arterial hypertension. European
- 621 *respiratory review* 23, 476–487
- Nash, M. P. and Hunter, P. J. (2000). Computational mechanics of the heart. Journal of elasticity and the
- 623 physical science of solids 61, 113–141
- 624 Odeigah, O. O., Valdez-Jasso, D., Wall, S. T., and Sundnes, J. (2022). Computational models of ventricular
- mechanics and adaptation in response to right-ventricular pressure overload. Frontiers in Physiology 13,
- 626 948936
- Pang, Q.-Y., An, R., and Liu, H.-L. (2018). Effects of inhalation and intravenous anesthesia on intraoperative
- 628 cardiopulmonary function and postoperative complications in patients undergoing thoracic surgery.
- 629 Minerva Anestesiologica 84, 1287–1297
- 630 Quaife, R. A., Chen, M. Y., Lynch, D., Badesch, D. B., Groves, B. M., Wolfel, E., et al. (2006). Importance
- of right ventricular end-systolic regional wall stress in idiopathic pulmonary arterial hypertension: a new
- 632 method for estimation of right ventricular wall stress. European journal of medical research 11, 214
- 633 Rain, S., Andersen, S., Najafi, A., Gammelgaard Schultz, J., da Silva Gonçalves Bós, D., Handoko, M. L.,
- et al. (2016). Right ventricular myocardial stiffness in experimental pulmonary arterial hypertension:
- relative contribution of fibrosis and myofibril stiffness. Circulation: Heart Failure 9, e002636
- 636 Rain, S., Handoko, M. L., Trip, P., Gan, C. T.-J., Westerhof, N., Stienen, G. J., et al. (2013). Right
- ventricular diastolic impairment in patients with pulmonary arterial hypertension. Circulation 128,
- 638 2016–2025
- 639 Scollan, D., Holmes, A., Zhang, J., and Winslow, R. (2000). Reconstruction of cardiac ventricular geometry
- and fiber orientation using magnetic resonance imaging. *Annals of biomedical engineering* 28, 934–944
- 641 Shanno, D. F. (1970). Conditioning of quasi-newton methods for function minimization. Mathematics of
- 642 *computation* 24, 647–656
- 643 Strauer, B.-E. (1979). Myocardial oxygen consumption in chronic heart disease: role of wall stress,
- 644 hypertrophy and coronary reserve. *The American journal of cardiology* 44, 730–740
- 645 Streeter Jr, D. D., Spotnitz, H. M., Patel, D. P., Ross Jr, J., and Sonnenblick, E. H. (1969). Fiber orientation
- in the canine left ventricle during diastole and systole. Circulation research 24, 339–347
- 647 Suga, H. and Sagawa, K. (1974). Instantaneous pressure-volume relationships and their ratio in the excised,
- supported canine left ventricle. Circulation research 35, 117–126
- 649 Suga, H., Sagawa, K., and Shoukas, A. A. (1973). Load independence of the instantaneous pressure-
- volume ratio of the canine left ventricle and effects of epinephrine and heart rate on the ratio. *Circulation*
- 651 research 32, 314–322
- 652 Sundnes, J., Wall, S., Osnes, H., Thorvaldsen, T., and McCulloch, A. D. (2014). Improved discretisation
- and linearisation of active tension in strongly coupled cardiac electro-mechanics simulations. *Computer*
- 654 methods in biomechanics and biomedical engineering 17, 604–615

655 Swift, A. J., Capener, D., Johns, C., Hamilton, N., Rothman, A., Elliot, C., et al. (2017). Magnetic resonance

- 656 imaging in the prognostic evaluation of patients with pulmonary arterial hypertension. *American journal*
- of respiratory and critical care medicine 196, 228–239
- 658 Taraseviciene-Stewart, L., Kasahara, Y., Alger, L., Hirth, P., MAHON, G. M., Waltenberger, J., et al.
- 659 (2001). Inhibition of the vegf receptor 2 combined with chronic hypoxia causes cell death-dependent
- pulmonary endothelial cell proliferation and severe pulmonary hypertension. The FASEB Journal 15,
- 661 427–438
- 662 Templeton, G. H., Ecker, R. R., and Mitchell, J. H. (1972). Left ventricular stiffness during diastole and
- systole: the influence of changes in volume and inotropic state. Cardiovascular Research 6, 95–100
- 664 Trip, P., Rain, S., Handoko, M. L., Van der Bruggen, C., Bogaard, H. J., Marcus, J. T., et al. (2015). Clinical
- relevance of right ventricular diastolic stiffness in pulmonary hypertension. European Respiratory
- 666 Journal 45, 1603–1612
- van Wolferen, S. A., Marcus, J. T., Boonstra, A., Marques, K. M., Bronzwaer, J. G., Spreeuwenberg, M. D.,
- et al. (2007). Prognostic value of right ventricular mass, volume, and function in idiopathic pulmonary
- arterial hypertension. European heart journal 28, 1250–1257
- 670 Vélez-Rendón, D., Pursell, E. R., Shieh, J., and Valdez-Jasso, D. (2019). Relative contributions of matrix
- and myocytes to biaxial mechanics of the right ventricle in pulmonary arterial hypertension. *Journal of*
- 672 Biomechanical Engineering 141, 091011
- 673 Vélez-Rendón, D., Zhang, X., Gerringer, J., and Valdez-Jasso, D. (2018). Compensated right ventricular
- function of the onset of pulmonary hypertension in a rat model depends on chamber remodeling and
- 675 contractile augmentation. *Pulmonary circulation* 8, 2045894018800439
- 676 Virtanen, P., Gommers, R., Oliphant, T. E., Haberland, M., Reddy, T., Cournapeau, D., et al. (2020). Scipy
- 1.0: fundamental algorithms for scientific computing in python. *Nature methods* 17, 261–272
- 678 Voelkel, N. F., Gomez-Arroyo, J., Abbate, A., Bogaard, H. J., and Nicolls, M. R. (2012). Pathobiology
- of pulmonary arterial hypertension and right ventricular failure. European Respiratory Journal 40,
- 680 1555–1565
- Vonk-Noordegraaf, A., Haddad, F., Chin, K. M., Forfia, P. R., Kawut, S. M., Lumens, J., et al. (2013).
- Right heart adaptation to pulmonary arterial hypertension: physiology and pathobiology. Journal of the
- 683 American College of Cardiology 62, D22–D33
- Vonk Noordegraaf, A., Westerhof, B. E., and Westerhof, N. (2017). The relationship between the right
- ventricle and its load in pulmonary hypertension. Journal of the American College of Cardiology 69,
- 686 236–243
- 687 Xi, J., Lamata, P., Lee, J., Moireau, P., Chapelle, D., and Smith, N. (2011). Myocardial transversely
- isotropic material parameter estimation from in-silico measurements based on a reduced-order unscented
- 689 kalman filter. Journal of the mechanical behavior of biomedical materials 4, 1090–1102
- 690 Yang, C.-F., Chen, M. Y.-C., Chen, T.-I., and Cheng, C.-F. (2014). Dose-dependent effects of isoflurane on
- 691 cardiovascular function in rats. *Tzu Chi Medical Journal* 26, 119–122

Table 1. Right ventricular wall thicknesses and cavity volumes used to build the computational meshes.

Case	Wall thickness, mm	Cavity volume, $\mu \mathbf{L}$
Control	0.8	170
SuHx Week 4	1.6	187
SuHx Week 8	1.8	202
SuHx Week 12	1.9	308

LV wall thickness and cavity volume were fixed to 2 mm and 165 μ L respectively for all cases.

Table 2. Optimized passive material parameter.

Case	LV passive material parameter, kPa	RV passive material parameter, kPa	
Control		0.07	
SuHx Week 4	1 40 6 11	0.22	
SuHx Week 8	1.42 for all cases	0.23	
SuHx Week 12		0.18	

Table 3. Mesh resolution, cost functional evaluation (eval) time, number of cost functional evaluations, and total run time of the optimization process for the different cases.

Case	No. of mesh elements	Functional eval time, seconds	No. of functional evaluations	Total run time, hours
Control	39 294	465.9 ± 236.2	6 ± 2	39
SuHx Week 4	43 995	596.5 ± 235.9	7 ± 2	52
SuHx Week 8	45 564	661.1 ± 287.4	7 ± 3	58
SuHx Week 12	49 910	895.3 ± 328.1	5 ± 2	64

Cost functional evaluation time and number of cost functional evaluations are average values for optimizing one measurement (i.e., pressure-volume) point of the data shown in Figure 3 along with standard deviations.

Table 4. Model-predicted end-diastolic (E_{ed}) and end-systolic (E_{es}) elastance compared with published group means \pm standard error (SE).

Case	$\mathbf{E_{ed}}$ (Group mean \pm SE), mmHg/ μ L	$\mathbf{E_{es}}$ (Group mean \pm SE), mmHg/ μ L
Control	$0.03~(0.017\pm0.002)$	$0.29~(0.30\pm0.033)$
SuHx Week 4	$0.06 (0.036 \pm 0.01)$	$0.52~(0.39\pm0.08)$
SuHx Week 8	$0.11~(0.13\pm0.02)$	$0.55~(0.85\pm0.13)$
SuHx Week 12	$0.13~(0.06\pm0.02)$	$0.26~(0.76\pm0.1)$

Group means \pm SE shown for SuHx Week 12 are for week 10 animals, because the published study did not include week 12 animals.

Table 5. Model predictions of average right ventricular free wall stress.

	Control	SuHx		
		Week 4	Week 8	Week 12
ED fiber stress, kPa	0.36	0.95	1.58	2.70
ES fiber stress, kPa	14.48	16.38	20.33	20.78
Peak fiber stress, kPa	22.18	16.46	20.47	22.34
ED circumferential stress, kPa	0.20	0.80	1.53	2.80
ES circumferential stress, kPa	9.84	9.59	12.19	14.98
Peak circumferential stress, kPa	20.39	13.08	17.24	16.80
ED AOT stress, kPa	0.02	0.39	0.70	0.98
ES AOT stress, kPa	5.59	5.76	7.30	6.93
Peak AOT stress, kPa	11.54	6.65	8.23	7.81
ED fiber strain	0.14	0.14	0.16	0.20
ES fiber strain	0.0002	0.01	0.02	0.10
Peak fiber strain	0.18	0.22	0.27	0.29
ED circumferential strain	0.27	0.28	0.34	0.39
ES circumferential strain	0.01	0.05	0.08	0.21
Peak circumferential strain	0.36	0.42	0.51	0.51
ED AOT strain	0.10	0.09	0.09	0.11
ES AOT strain	0.008	0.016	0.008	0.05
Peak AOT strain	0.20	0.16	0.15	0.15

Abbreviations: ED, end diastole; ES, end systole; AOT, apex-to-outflow; SuHx, sugen-hypoxia.